Nanoporous Materials Very Important Paper

Deutsche Ausgabe: DOI: 10.1002/ange.201612041
Internationale Ausgabe: DOI: 10.1002/anie.201612041

Highly Porous Thermoelectric Nanocomposites with Low Thermal Conductivity and High Figure of Merit from Large-Scale Solution-Synthesized $Bi_2Te_{2.5}Se_{0.5}$ Hollow Nanostructures

*Biao Xu, Tianli Feng, Matthias T. Agne, Lin Zhou, Xiulin Ruan, G. Jeffery Snyder, and Yue Wu**

Abstract: *To enhance the performance of thermoelectric materials and enable access to their widespread applications, it is beneficial yet challenging to synthesize hollow nanostructures in large quantities, with high porosity, low thermal conductivity (κ) and excellent figure of merit (z T). Herein we report a scalable (ca. 11.0 g per batch) and low-temperature colloidal processing route for $Bi_2Te_{2.5}Se_{0.5}$ hollow nanostructures. They are sintered into porous, bulk nanocomposites (phi 10 mm × h 10 mm) with low κ ($0.48\,W\,m^{-1}\,K^{-1}$) and the highest z T (1.18) among state-of-the-art $Bi_2Te_{3-x}Se_x$ materilas. Additional benefits of the unprecedented low relative density (68–77 %) are the large demand reduction of raw materials and the improved portability. This method can be adopted to fabricate other porous phase-transition and thermoelectric chalcogenide materials and will pave the way for the implementation of hollow nanostructures in other fields.*

Hollow nanostructures have attracted continuously interest in diverse fields, such as batteries,[1] supercapacitors,[2] biomedicine,[3] catalysis,[4] photocatalysis,[5] sensors,[6] and optics,[7] because their hollow interiors can act as containers and provide a large number of reactive sites due to their high specific surface area.[8] To synthesize hollow nanostructures, hard-templating (e.g. against silica nanoparticles[9] or polystyrene nanobeads[10]) and self-templating (e.g. Kirkendall effect[11]) are widely investigated. The self-templating synthesis is more straightforward and easier to scale up. The large-scale production, in conjunction with exploring how to use the hollow nanostructures, can lead to their practical implementation.

Solid-state semiconductors can convert waste heat into electric power through the thermoelectric effect. Thermoelectric devices exhibit excellent reliability and portability, representing a promising method of energy recovery.[12] The performance of a thermoelectric material is determined by its figure of merit, $zT = S^2\sigma T/\kappa$, where S is the Seebeck coefficient, σ is the electrical conductivity, and κ is the thermal conductivity. Recently, nanostructures have been extensively used to lower the κ and improve the zT of the thermoelectric materials.[13] It can be ascribed to the increased scattering of phonons with increasing grain boundary density. However, due to the commonly used high-temperature processes required to fabricate thermoelectric modules, grain growth is unavoidable, diminishing the structural effect on κ. Alternatively, porosity that arises from the irregular shape and imperfect stacking of building blocks at the nanoscale can offer an additional means to reduce the thermal conductivity, yet limitedly.[14] To further increase the porosity of a thermoelectric material, it might be an effective way to use hollow nanostructure as a powder precursor, as it intrinsically holds a large amount of void spaces. However, hollow nanostructures have been seldom used as thermoelectric materials due to the concern of significantly sacrificed electrical conductivity.[15] There has not been any complete evaluation of the figure of merit on the bulk scale (> 10 g).

Herein, we report the first example of the scalable (ca. 11 g per batch), self-templating synthesis of $Bi_2Te_{2.5}Se_{0.5}$ hollow nanostructures and the subsequent sintering of them into highly porous thermoelectric nanocomposites. The as-sintered material is 32 % porous and holds an ultralow thermal conductivity. Consequently, its zT is comparable to the best $Bi_2Te_{3-x}Se_x$. This approach can reduce the demand in raw material and provide better portability due to the light weight compared to conventional fully dense thermoelectric materials.

The multistep synthesis is inspired by our previous method to synthesize Bi_2Te_3 nanowires.[16] In step 1, tellurium dioxide (TeO_2), selenium dioxide (SeO_2), potassium hydroxide (KOH), and polyvinylpyrrolidone (PVP) were dissolved into ethylene glycol (EG). Then hydrazine hydrate ($N_2H_4{\cdot}H_2O$) was injected and the solution turned dark blue. This mixture was heated at 110 °C for 1 h, for the formation of Te-Se nanorods (Figure 1 a). In step 2, anhydrous hydrazine (N_2H_4) and a stock solution of $Bi(NO_3)_3{\cdot}5\,H_2O$ were injected into this dispersion sequentially to form the Bi-Te-Se nanorods (Figure 1 b). This dispersion was heated at 110 °C for another hour. In step 3, the temperature was raised to 140 °C and maintained for 3 h to yield BiTeSe hollow nanorods (Figure 1 c).

To characterize the intermediate products, several investigations were conducted. First, X-ray diffraction (XRD) was used to study the crystal phases. After step 1, the product

---

[*] Dr. B. Xu, Prof. Dr. Y. Wu
Department of Chemical and Biological Engineering
Iowa State University, Ames, IA 50011 (USA)
E-mail: yuewu@iastate.edu

T. L. Feng, Prof. Dr. X. L. Ruan
Department of Mechanical Engineering, Purdue University
West Lafayette, IN 47907 (USA)

M. T. Agne, Prof. Dr. G. J. Snyder
Department of Materials Science and Engineering
Northwestern University, Evanston, IL 60208 (USA)

Dr. B. Xu, Prof. Dr. L. Zhou, Prof. Dr. Y. Wu
Ames Laboratory, Department of Energy
Ames
IA 50011 (USA)

Supporting information for this article can be found under: http://dx.doi.org/10.1002/anie.201612041.

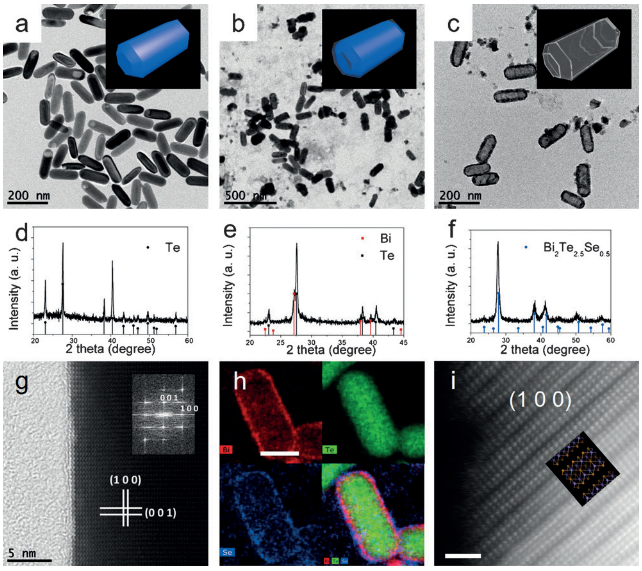

Figure 1. Low-magnification TEM images of a) Te nanorods (step 1), b) Te@Bi-Se core–shell nanorods (step 2), and c) $Bi_2Te_{2.5}Se_{0.5}$ hollow nanorods (step 3), d–f) XRD profiles of the products in each step, g) HRTEM image of the Te nanorods, h) EDS elemental mapping of the Te@Bi-Se core–shell nanorods, scale bar 50 nm, i) C_s-corrected HAADF-STEM image of the $Bi_2Te_{2.5}Se_{0.5}$ hollow nanostructures and the corresponding atomic model of (100) surface, Bi, purple, Te(Se), orange, scale bar 1 nm.

could be indexed to pure trigonal tellurium (JCPDS number 36-1452, Figure 1 d). After step 2, hexagonal bismuth (JCPDS number 44-1246) was found because anhydrous hydrazine-reduced $Bi^{III}(NO_3)_3$ to Bi^0. Meanwhile, Te^0 was still retained (Figure 1 e). Finally, in step 3, Bi and Te (Se) reacted with each other to form hexagonal $Bi_2Te_{2.5}Se_{0.5}$ (JCPDS number 51-0643, Figure 1 f). Transmission electron microscopy (TEM) provided more details about the microstructures of these intermediate products. After step 1, Te nanorods were formed (Figure 1 a). Statistics on multiple nanorods revealed that the length was 150 ± 10 nm and the diameter was 50 ± 4 nm. The (001) plane was found to be perpendicular to the axial direction of the nanorod (Figure 1 g). After step 2, the surface of the nanorods became very rough (Figure 1 b). The length was elongated to 170 ± 15 nm and the diameter was enlarged to 60 ± 8 nm. Combining the increased size of the nanorods with the result of XRD ($Bi^0 + Te^0$, Figure 1 e), we speculated that Bi^0 had deposited onto the surface of the Te nanorod. Energy dispersive spectroscopy (EDS) elemental mapping apparently proved that the core was composed of Te while the shell was comprised of Bi and Se (Figure 1 h). After step 3, all the nanorods were found to transform to hollow shells. The outer diameter was 60 ± 8 nm, the length was 180 ± 15 nm and the average thickness of the shell was 12 ± 3 nm (Figure 1 c). EDS elemental mapping indicated that Bi, Te, and Se were uniformly distributed in the hollow nanostructure (see Figure S1 f in the Supporting Information). At the tip ends, the (006) plane of $Bi_2Te_{2.5}Se_{0.5}$ was observed perpendicular to the axial direction (Figure S1 e). The atomic structure can be clearly depicted in the C_s-corrected HAADF STEM image, when referred to a proposed atomic structure of $Bi_2Te_{2.5}Se_{0.5}$ (100) in Figure 1 i.

Scanning electron microscopy (SEM) further verified the morphologies of the products step by step (Figure S2). Additionally, EDS revealed the compositions of these products. After step 1, the atomic ratio of Te:Se was 96.0:4.0. According to the precursor ratio of Te:Se (83.33:16.67), Se was only partially (ca. 1/5) converted. After step 2, Bi:Te:Se = 37.64:51.64:10.69. [Te + Se]/Bi = 1.66, while the nominal ratio was 1.50, indicating that Bi was deficient in the product. In this Te@Bi-Se core–shell structure, Te:Se = 4.83:1, which was quite close to the nominal ratio of 5:1. After step 3, Bi:Te:Se = 41.22:50.23:9.54. [Te + Se]/Bi = 1.45, which was nearly the same as the nominal 1.50 ratio. In this final $Bi_2Te_{2.5}Se_{0.5}$ hollow nanostructure, Te:Se = 5.27:1 and this was also approximate to 5:1 of the precursors.

Based on the aforementioned characterizations, we attempted to clarify the formation mechanisms of the $Bi_2Te_{2.5}Se_{0.5}$ hollow nanorod. As stated before, after the 2nd step, the Te@Bi-Se (core@shell) structure was formed. We found that a small portion of them transformed to a partially hollow structure (Figure S1b and d). In this intermediate structure, the Te-Se core nanorod reacted and became concaved in the equatorial region. The corresponding region of the shell showed a layered structure of $Bi_2(Te_xSe_{1-x})_3$ (Figure S1d), indicating that the reaction between Bi and Te (Se) had started. To form the $Bi_2(Te_xSe_{1-x})_3$ shell, Te atoms had to diffuse outward and Bi(Se) atoms inward across the interface, reacting with each other. The Kirkendall effect might play a role in this process. Generally, the diffusion flow is expressed as follows Equation (1),[17]

$$|J_i| = \frac{D_i \Delta C_i}{r^2} \frac{r_{\mathrm{in}}(t) r_{\mathrm{out}}(t)}{r_{\mathrm{out}}(t) - r_{\mathrm{in}}(t)} \qquad (1)$$

where J_i is the magnitude of the flux, D_i is the diffusion coefficient, ΔC_i is the difference of concentration across the interface, for species i, r_{in} and r_{out} are the diameters of the inner (Te/Bi_2Te_3) and outer interface (Bi_2Te_3/Bi), respectively. As the atomic radius of Te (140 pm) is much smaller than that of Bi (160 pm), D_{Te} could be larger than D_{Bi}. Moreover, to form stoichiometric Bi_2Te_3, three atoms of Te had to diffuse out and only two of Bi in. As the initial $\Delta C_{\mathrm{Te}}:\Delta C_{\mathrm{Bi}}$ was 3:2 (determined by precursors), this ratio would be maintained as 3:2. Therefore, $J_{\mathrm{Te,out}}$ should be larger than $J_{\mathrm{Bi,in}}$ throughout the process and the inner core of Te would become void during the diffusion–reaction process (Figure S1c). Finally, during the 3rd step, as the temperature was increased to 140 °C, the diffusion and reaction were completed. Resultantly, all the nanorods became hollow.

The scalable (11.0 g, Figure 2 a) synthesis of $Bi_2Te_{2.5}Se_{0.5}$ hollow nanostructures enabled us to fabricate bulk nanocomposites and study their thermoelectric properties. The as-obtained dispersion of hollow nanorods was centrifuged, dried under vacuum, and pulverized. This powder was spark plasma sintered (SPSed) into a phi-10 mm cylinder and a pellet (Figure 2 b). For the 400 °C-sintered sample, the mass density was 5.30 g cm^{-3} and the relative density was 67.9 %, among the lowest reported for $Bi_2Te_{3-x}Se_x$-based

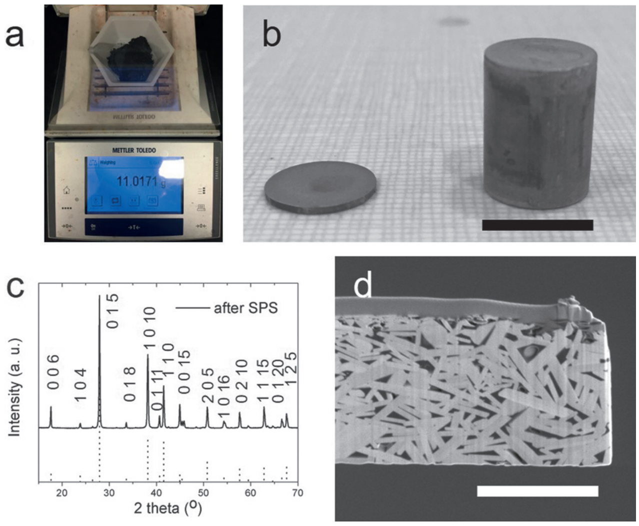

Figure 2. a) 11.0 g of the hollow nanostructure product, b) 400 °C-sintered pellet and cylinder, scale bar 10 mm, c) XRD profile of the 400 °C-sintered pellet, d) SEM of the FIB-cut specimen from the 400 °C-sintered disk, scale bar 2 μm.

thermoelectric materials (Table 1). For the 350 °C-sintered sample, the mass density was 6.02 g cm^{-3} and the relative density was 77.2 %. The as-sintered nanocomposite was then comprehensively characterized. The XRD profile showed typical reflection peaks of $Bi_2Te_{2.5}Se_{0.5}$ (JCPDS number 51-0643, Figure 2 c). EDS confirmed a composition of $Bi_{2.02}Te_{2.56}Se_{0.44}$. From the SEM image of a focused-ion-beam (FIB) cut sample (Figure 2 d), we found that the starting nanoshells were crushed and re-pressed into a highly porous material with larger grains.

The thermoelectric properties of the SPSed $Bi_{2.02}Te_{2.56}Se_{0.44}$ nanocomposites were then measured along the out-of-plane direction and the results were shown in Figure 3. The electrical conductivities (σ) of the 350 °C- and 400 °C-sintered samples were displayed in Figure 3 a. For the 400 °C-sintered sample, σ decreased from $8.13\times10^4\ \mathrm{S\,m^{-}}$ at 313 K, monotonically with increasing temperature, to $4.93\times10^4\ \mathrm{S\,m^{-}}$ at 513 K. This indicated the behavior of a degenerate semiconductor. The carrier concentration was extracted through Hall effect measurement ($n_H\approx7.0\times10^{19}\ \mathrm{cm^{-3}}$, Figure S3a). Hall coefficient was negative and nearly constant, confirming that our nanocomposite was heavily doped to n-type. Electron mobility μ was calculated as $\mu=\sigma/n_H e$ and exhibited in Figure S3b.

The Seebeck coefficient (S) had a negative sign, agreeing well with the Hall effect measurement. The absolute value of S increased monotonically with respect to temperature (Figure 3 a). However, the slope became smaller and a plateau in S was achieved in the high-temperature range. This is typical of bipolar conduction, where thermal excitation of the minority carriers (hole) contributes negatively to the total S. The power factor was calculated as $S^2\sigma$ (Figure 3 b). Throughout the temperature of interest, $S^2\sigma$ of the 400 °C-sintered sample showed a very small change and the peak value was 1.28 mW m^{-1} K^{-2} at 438 K. The total thermal conductivity was calculated through $\kappa_{tot}=D_T C_p \rho$, where D_T (thermal diffusivity) could be measured from the laser flash method (Figure S3c), C_p (specific heat) was obtained by a differential scanning calorimeter (DSC, Figure S3d) and ρ (density) was determined from the mass and geometry. The temperature dependence of κ_{tot} is displayed in Figure 3 b. For the 400 °C-sintered sample, κ_{tot} decreased from 0.66 W m^{-1} K^{-1} at 313 K to 0.59 W m^{-1} K^{-1} at 438 K, and then increased again to 0.62 W m^{-1} K^{-1}at 538 K. For the 350 °C-sintered sample, κ_{tot} achieved its minimum value of 0.48 W m^{-1} K^{-1} at 438 K.

Table 1: Properties of our $Bi_2Te_{3-x}Se_x$ materials as compared with literature values.

	Sintering condition	Relative density	$\kappa_{lat,min}$ [W m^{-1} K^{-1}]	Carrier mobility [cm^2 V^{-1} s^{-1}]	$\mu_H/\kappa_L\cdot(m^*/m^0)^{3/2}$ [10^{-3} m^3 K V^{-1} s^{-1} W^{-1}]	zT_{max}
This work	400 °C, 40 MPa, 5 min	**67.9 %**	**0.13**	71 (313 K)	19.5 (313 K)	1.00 (488 K)
	350 °C, 40 MPa, 5 min	**77.2 %**	**0.14**	68 (313 K)	17.3 (313 K)	**1.18** (463 K)
Ren, 2010[18]	500 °C, 2 min	87 %	N/A	N/A	N/A	1.04 (398 K)
Xiong, 2012[19]	250 °C, 40 MPa, 5 min	87 %	0.45	N/A	N/A	0.55 (300 K)
Zhao, 2015[20]	400 °C, 80 MPa, 30 min	97 %	0.52	157 (300 K)	56 (300 K)	1.20 (360 K)
Li, 2016[21]	460 °C, 50 MPa, 5 min	97 %	0.40	152 (300 K)	30 (300 K)	1.10 (470 K)
Zou, 2016[22]	250 °C, 40 MPa, 5 min	92.6 %	0.36	250 (300 K)	N/A	1.23 (470 K)

Finally, zT is calculated as $S^2\sigma T\kappa^{-1}$ and its temperature dependence is plotted in Figure 3 d. For the 350 °C-sintered sample, the zT at 313 K is 0.61 and increases steadily with temperature, reaching the peak of 1.18 at 463 K. The zT of >1.0 is maintained from 388 K to 513 K. For the 400 °C-sintered sample, the highest zT also reaches 1.0.

We then conduct theoretical modeling to clarify the origin of the decent figure of merit of our porous BiTeSe nanocomposite. It is mainly ascribed to the high porosity and low thermal conductivity.

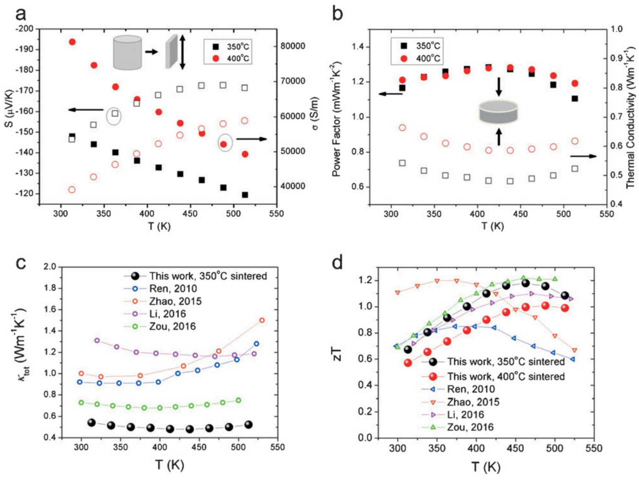

Figure 3. Temperature dependence of a) Seebeck coefficients (S, hollow markers) and electrical conductivities (σ, solid markers), b) power factors ($S^2\sigma$, solid markers) and thermal conductivities (κ_{tot}, hollow markers). c) κ_{tot} and d) zT of the porous nanocomposite in this work compared with previously reported $Bi_2Te_{3-x}Se_x$.[18–22] Also see Table 1 for more details.

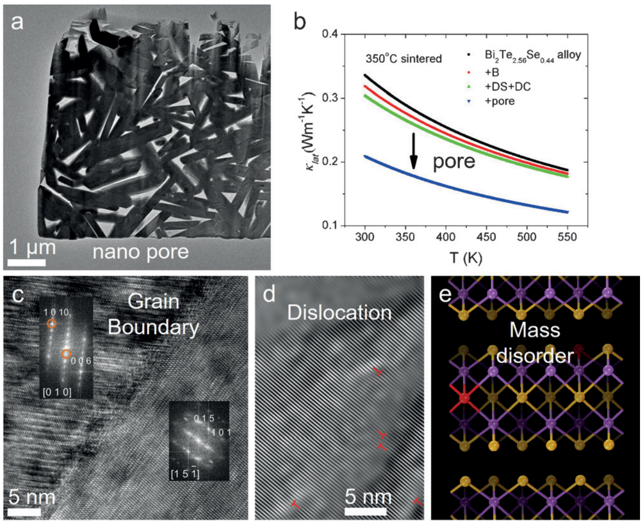

Figure 4. a) TEM image of the porous $Bi_{2.02}Te_{2.56}Se_{0.44}$ nanocomposite (400 °C-sintered), b) theoretical modeling of $\kappa_{\mathrm{lattice}}$ of the 350 °C-sintered BiTeSe nanocomposite, c) HRTEM image showing a grain boundary, d) inverse fast Fourier transform (IFFT) of a HRTEM image showing dislocations, e) scheme on alloy mass disorder; bismuth (purple), tellurium (orange), and selenium (red).

Based on the effective medium theory,[23] the lattice thermal conductivity of a porous material is expressed in Equation (2),

$$\kappa_l = (1-P)^{3/2}\kappa_{l,f} \tag{2}$$

where $\kappa_{l,f}$ is the lattice thermal conductivity of the imaginary fully dense material, P is the porosity ($P=1-\rho/\rho_0$, ρ/ρ_0 is the relative density). For our 400 °C-sintered sample, $\kappa_l=\kappa_{l,f}/1.78$ (Figure 4 b). The lattice thermal conductivity of the imaginary fully dense nanocomposite $\kappa_{l,f}$ is then calculated by the phonon Boltzmann transport Equation (3).[24]

$$\kappa_{l,f} = \frac{4\pi}{3}\frac{1}{(2\pi)^3}\sum_j\left[\frac{2}{3}\int_x+\frac{1}{3}\int_z\right]\frac{\hbar^2\omega^2(\mathbf{k},j)}{k_BT^2}\frac{e^{\frac{\hbar\omega(\mathbf{k},j)}{k_BT}}}{\left(e^{\frac{\hbar\omega(\mathbf{k},j)}{k_BT}}-1\right)^2} \tag{3}$$
$$\cdot\nu^2(\mathbf{k},j)\tau_{\mathrm{ph}}(\mathbf{k},j)k^2dk$$

To obtain $\kappa_{l,f}$ with Equation (3), we need to know the phonon frequency ω, the phonon group velocity v, and the phonon relaxation time τ_{ph} at the wave-vector $\mathbf{k}$ and branch j. ω and v are obtained from first principles calculations using density functional theory (DFT),[25] and τ_{ph} is calculated from the Matthiessen rule in Equation (4).

$$\tau_{\mathrm{ph}}^{-1}(\mathbf{k},j)=\tau_{\mathrm{anh}}^{-1}(\mathbf{k},j)+\tau_{\mathrm{mass}}^{-1}(\mathbf{k},j)+\tau_{\mathrm{coupl}}^{-1}(\mathbf{k},j)+\tau_{\mathrm{DC}}^{-1}(\mathbf{k},j) \tag{4}$$
$$+\tau_{\mathrm{DS}}^{-1}(\mathbf{k},j)+\tau_{\mathrm{B}}^{-1}(\mathbf{k},j)$$

The terms on the right hand side are the scattering rates induced by the lattice anharmonicity (anh), Te-Se alloy mass disorder (mass), coupling between anharmonic phonon scattering and mass disorder scattering (coupl), dislocation core (DC), dislocation strain (DS), and grain boundaries (B), respectively. The detailed calculations of them can be found in the Supporting Information. The parameters involved were determined from various experiments (Table S1). The lattice anharmonicity was extracted from a previous study on bulk-grain Bi_2Te_3 and Bi_2Se_3.[26] The extent of Te-Se mass disorder was determined from EDS. Dislocations were observed from TEM (Figure 4 d). The dislocation densities were 5.0×10^{11} cm^{-2} and 7.6×10^{11} cm^{-2}, for the 350 °C- and 400 °C-sintered sample, respectively. Grain boundary was also studied by TEM (Figure 4 c). Low-magnification TEM (Figure 4 a) and SEM images (Figure S2d) revealed that the grains were big flakes with diameter around 1.5 μm for the 400 °C-sintered sample (1.2 μm for the 350 °C-sintered one) and thickness around 300 nm for the 400 °C-sintered sample (250 nm for the 350 °C-sintered one).

Based on the modeling, we have found that the ultralow lattice thermal conductivity is benefited from the broad-range phonon frequency scattering and the large porosity. At 463 K where zT reached its maxima for the 350 °C-sintered sample, the lattice thermal conductivity of bulk-grain $Bi_2Te_{2.56}Se_{0.44}$ (0.71 W m^{-1} K^{-1}) was reduced by the grain boundary, dislocation, mass-disorder and coupling scatterings to 0.21 W m^{-1} K^{-1}, which was then further diminished by the pores (Figure 4 a) to 0.14 W m^{-1} K^{-1} (Figure 4 b). Due to the extremely low relative density and high porosity (Table 1), the κ_{lat} of our material was very low (Table 1; lat = lattice). Consequently, the κ_{total} of our highly porous BiTeSe is also the lowest among those in literatures[18–22] (Figure 3 c), from RT to 513 K. Although the dislocation, grain boundary, and pores had reduced the lattice thermal conductivity to a large extent, the electron mobility of our porous BiTeSe material was still maintained quite high (Table 1), possibly due to the large grain size and high crystallinity. Thus, the quality factor, $\mu_{\mathrm{H}}/$

$\kappa_L\cdot(m^*/m^0)^{3/2}$, was as high as those of previously reported BiTeSe[21] (Table 1) and the zT of our highly porous BiTeSe nanocomposite (350 °C-sintered) was higher than 1.0 from 388 to 513 K, making it suitable for converting waste heat to electricity.

Compared with state-of-the-art n-type BiTeSe materials, our highly porous BiTeSe nanocomposite has comparable or even higher zT but uses nearly 1/3 less quantity of expensive raw materials (namely tellurium), reducing the overall production costs. Additionally, the extremely low mass density (67.9% or 77.2%) further enhances the portability of the thermoelectric module. These two advantages make our material suitable in practical use (e.g. powering wearable electronics) and niche application (e.g. power source in deep-space emission), respectively. Lastly, we emphasize that the low-temperature solution processing method is energy-saving when compared to the high-T solid-state route commonly used in making other n-type materials, such as MgSiSn[27] and NaGaSn,[28] that are used in the same temperature range (300–500 K).

In conclusion, we have synthesized $Bi_2Te_{2.5}Se_{0.5}$ hollow nanostructures using a scalable (11.0 g) solution-phase route. The as-obtained nanopowder can be spark-plasma-sintered into a highly porous nanocomposite that exhibits a $zT > 1$ in a wide temperature range (388–513 K). Through theoretical modeling, we find that the distinctly high porosity, as well as grain boundary, dislocation, and alloy mass disorder, lead to the extremely low thermal conductivity and high figure of merit. The ultralow relative density will also reduce the use of raw materials and improve the portability of the thermoelectric device. We expect that this approach can be readily adopted to fabricate other types of porous phase-transition and thermoelectric chalcogenide nanocomposites, such as Ag_2Te, Cu_2Te, PbTe, PbSe, and SnSe, and facilitate the use of hollow nanostructures in a variety of fields.

Acknowledgements

B.X. and Y.W. gratefully thank for support from the Office of Naval Research, award number N00014-16-1-2066. T.L.F. and X.L.R. acknowledge the Defense Advanced Research Projects Agency (DARPA), award number HR0011-15-2-0037. M.T.A. and J.G.S. would like to acknowledge funding from the Solid-State Solar-Thermal Energy Conversion Centre (S3TEC), an Energy Frontier Research Centre funded by the U.S. Department of Energy, Office of Science, Basic Energy Sciences under award number DE-SC0001299. The TEM work (L.Z.) was performed at the Ames Laboratory under contract number DE-AC02-07CH11358 which is supported by the Materials Sciences Division of the Office of Basic Energy Sciences of the U.S. Department of Energy.

Conflict of interest

The authors declare no conflict of interest.

Keywords: hollow nanostructures · Kirkendall effect · porous nanocomposites · thermal conductivity · thermoelectric materials

How to cite: *Angew. Chem. Int. Ed.* **2017**, *56*, 3546–3551
Angew. Chem. **2017**, *129*, 3600–3605

[1] X. W. Lou, Y. Wang, C. Yuan, J. Y. Lee, L. A. Archer, *Adv. Mater.* **2006**, *18*, 2325–2329.
[2] F. Xu, Z. Tang, S. Huang, L. Chen, Y. Liang, W. Mai, H. Zhong, R. Fu, D. Wu, *Nat. Commun.* **2015**, *6*, 7221.
[3] X. Cai, W. Gao, M. Ma, M. Wu, L. Zhang, Y. Zheng, H. Chen, J. Shi, *Adv. Mater.* **2015**, *27*, 6382–6389.
[4] S.-W. Kim, M. Kim, W. Y. Lee, T. Hyeon, *J. Am. Chem. Soc.* **2002**, *124*, 7642–7643.
[5] J. Sun, J. Zhang, M. Zhang, M. Antonietti, X. Fu, X. Wang, *Nat. Commun.* **2012**, *3*, 1139.
[6] H. Zhang, Q. Zhu, Y. Zhang, Y. Wang, L. Zhao, B. Yu, *Adv. Funct. Mater.* **2007**, *17*, 2766–2771.
[7] S. E. Skrabalak, L. Au, X. Li, Y. Xia, *Nat. Protoc.* **2007**, *2*, 2182–2190.
[8] X. Wang, J. Feng, Y. Bai, Q. Zhang, Y. Yin, *Chem. Rev.* **2016**, *116*, 10983–11060.
[9] J. B. Joo, Q. Zhang, M. Dahl, I. Lee, J. Goebl, F. Zaera, Y. Yin, *Energy Environ. Sci.* **2012**, *5*, 6321–6327.
[10] Z. Zhong, Y. Yin, B. Gates, Y. Xia, *Adv. Mater.* **2000**, *12*, 206–209.
[11] a) Y. Yin, R. M. Rioux, C. K. Erdonmez, S. Hughes, G. A. Somorjai, A. P. Alivisatos, *Science* **2004**, *304*, 711–714; b) H. Fan, M. Knez, R. Scholz, K. Nielsch, E. Pippel, D. Hesse, M. Zacharias, U. Gosele, *Nat. Mater.* **2006**, *5*, 627–631.
[12] a) W. G. Zeier, A. Zevalkink, Z. M. Gibbs, G. Hautier, M. G. Kanatzidis, G. J. Snyder, *Angew. Chem. Int. Ed.* **2016**, *55*, 6826–6841; *Angew. Chem.* **2016**, *128*, 6938–6954; b) J. R. Sootsman, D. Y. Chung, M. G. Kanatzidis, *Angew. Chem. Int. Ed.* **2009**, *48*, 8616–8639; *Angew. Chem.* **2009**, *121*, 8768–8792.
[13] a) B. Poudel, Q. Hao, Y. Ma, Y. Lan, A. Minnich, B. Yu, X. Yan, D. Wang, A. Muto, D. Vashaee, X. Chen, J. Liu, M. S. Dresselhaus, G. Chen, Z. Ren, *Science* **2008**, *320*, 634–638; b) K. F. Hsu, S. Loo, F. Guo, W. Chen, J. S. Dyck, C. Uher, T. Hogan, E. K. Polychroniadis, M. G. Kanatzidis, *Science* **2004**, *303*, 818–821; c) M. S. Dresselhaus, G. Chen, M. Y. Tang, R. G. Yang, H. Lee, D. Z. Wang, Z. F. Ren, J. P. Fleurial, P. Gogna, *Adv. Mater.* **2007**, *19*, 1043–1053; d) R. Tangirala, J. L. Baker, A. P. Alivisatos, D. J. Milliron, *Angew. Chem. Int. Ed.* **2010**, *49*, 2878–2882; *Angew. Chem.* **2010**, *122*, 2940–2944; e) D. Ding, D. Wang, M. Zhao, J. Lv, H. Jiang, C. Lu, Z. Tang, *Adv. Mater.* **2016**, DOI: 10.1002/adma.201603444.
[14] a) H. Lee, D. Vashaee, D. Z. Wang, M. S. Dresselhaus, Z. F. Ren, G. Chen, *J. Appl. Phys.* **2010**, *107*, 094308; b) Y. Zhang, T. Day, M. L. Snedaker, H. Wang, S. Krämer, C. S. Birkel, X. Ji, D. Liu, G. J. Snyder, G. D. Stucky, *Adv. Mater.* **2012**, *24*, 5065–5070.
[15] R. Jin, G. Chen, J. Pei, *J. Phys. Chem. C* **2012**, *116*, 16207–16216.
[16] S. W. Finefrock, H. Fang, H. Yang, H. Darsono, Y. Wu, *Nanoscale* **2014**, *6*, 7872–7876.
[17] Y. Yin, C. K. Erdonmez, A. Cabot, S. Hughes, A. P. Alivisatos, *Adv. Funct. Mater.* **2006**, *16*, 1389–1399.
[18] X. Yan, B. Poudel, Y. Ma, W. S. Liu, G. Joshi, H. Wang, Y. Lan, D. Wang, G. Chen, Z. F. Ren, *Nano Lett.* **2010**, *10*, 3373–3378.
[19] A. Soni, Z. Yanyuan, Y. Ligen, M. K. K. Aik, M. S. Dresselhaus, Q. Xiong, *Nano Lett.* **2012**, *12*, 1203–1209.
[20] L. Hu, H. Wu, T. Zhu, C. Fu, J. He, P. Ying, X. Zhao, *Adv. Energy Mater.* **2015**, *5*, 1500411.
[21] Y. Pan, J.-F. Li, *NPG Asia Mater.* **2016**, *8*, e275.
[22] M. Hong, T. C. Chasapis, Z.-G. Chen, L. Yang, M. G. Kanatzidis, G. J. Snyder, J. Zou, *ACS Nano* **2016**, *10*, 4719–4727.
[23] T. H. Bauer, *Int. J. Heat Mass Transfer* **1993**, *36*, 4181–4191.

[24] T. Feng, X. Ruan, *J. Nanomater.* **2014**, *2014*, 25.
[25] V. Chis, I. Y. Sklyadneva, K. A. Kokh, V. A. Volodin, O. E. Tereshchenko, E. V. Chulkov, *Phys. Rev. B* **2012**, *86*, 174304.
[26] W. Liu, K. C. Lukas, K. McEnaney, S. Lee, Q. Zhang, C. P. Opeil, G. Chen, Z. Ren, *Energy Environ. Sci.* **2013**, *6*, 552–560.
[27] W. Liu, X. Tan, K. Yin, H. Liu, X. Tang, J. Shi, Q. Zhang, C. Uher, *Phys. Rev. Lett.* **2012**, *108*, 166601.
[28] T. Yamada, H. Yamane, H. Nagai, *Adv. Mater.* **2015**, *27*, 4708–4713.

Manuscript received: December 10, 2016
Final Article published: January 12, 2017

Angewandte Chemie
Eine Zeitschrift der Gesellschaft Deutscher Chemiker

Supporting Information

Highly Porous Thermoelectric Nanocomposites with Low Thermal Conductivity and High Figure of Merit from Large-Scale Solution-Synthesized $Bi_2Te_{2.5}Se_{0.5}$ Hollow Nanostructures

*Biao Xu, Tianli Feng, Matthias T. Agne, Lin Zhou, Xiulin Ruan, G. Jeffery Snyder, and Yue Wu**

ange_201612041_sm_miscellaneous_information.pdf

Supporting information

Experimental Section

Large-Scale Synthesis

TeO_2 (99.995%), SeO_2 (99.999%), KOH (99.99%), polyvinylpyrrolidone (PVP, M_w = 40,000), ethylene glycol (99.0%), $N_2H_4 \cdot H_2O$ (80%), N_2H_4 (anhydrous, 98%) and $Bi(NO_3)_3 \cdot 5H_2O$ (99.99%) were purchased from Sigma Aldrich.

Step 1:

TeO_2 (37.5 mmol, 5.9850 g), SeO_2 (7.5 mmol, 0.8322 g), KOH (600 mmol, 33.66 g) and PVP (9.00 g, M_w = 40, 000) are dissolved into ethylene glycol (EG, 450 mL). This solution is heated to 110°C and then 7.5 mL of $N_2H_4 \cdot H_2O$ (80%) is injected. Then it is incubated at 110°C for 1h under nitrogen flow. For the synthesis of $Bi_2Te_{2.7}Se_{0.3}$, the amount of precursors should be changed to TeO_2 (40.5 mmol, 6.4638 g) and SeO_2 (4.5 mmol, 0.4993 g).

Step 2:

12 mL of N_2H_4 (anhydrous) and an EG (70 mL) solution containing $Bi(NO_3)_3 \cdot 5H_2O$ (30 mmol, 14.5520 g) are injected sequentially. Then the solution is maintained at 110°C for 1h under N_2.

Step 3:

The solution is heated to 140°C and kept at 140°C for 3h under nitrogen protection.

Spark Plasma Sintering

The colloidal dispersion is washed with water and centrifuged for 3 times. Then the precipitate is re-dispersed in an ethanol solution of 8% hydrazine hydrate and stirred for 24 h. After that, the dispersion is washed with ethanol and centrifuged for 2 times. Finally, the precipitate is dried in vacuum and ground into a fine powder.

This powder is mixed with 5% (w/w) of Te powder (~100 mesh, Sigma-Aldrich), loaded into a phi-10.0 mm graphite die and then set up in a Fuji-211lx spark plasma sintering (SPS) system. SPS condition is as follows: axial pressure 40 MPa, sintering temperature 350°C (or 400°C) and duration 5 min. After the sintering, the graphite die should be cooled down at a slow rate (20°C/min).

Characterizations

X-ray diffraction (XRD) is recorded on a Rigaku Ultima U4 diffractometer, with Cu Kα radiation (λ = 1.5418 Å), at 40 kV and 44 mA. Transmission Electron Microscopy (TEM) is acquired on a FEI Tecnai F20 at 200 kV and a FEI Titan Themis Cs-corrected TEM at 300 kV. Samples of the as-pressed BiTeSe pellet for HRTEM were prepared using a focused ion beam (FIB, Helios Dual Beam, FEI). Scanning Electron Microscopy (SEM) is conducted on a FEI Quanta 250, equipped with Energy Dispersion Spectra (EDS).

Thermoelectric Property

The Seebeck coefficients (S) are measured in a Linseis LSR-3. The electrical conductivity (σ) is also measured in a Linseis LSR-3 using a four-probe configuration and re-confirmed by a Van der-Pauw method. The thermal conductivity (κ) is expressed as $\kappa = D_T \cdot C_p \cdot \rho$. Thermal diffusivity ($D_T$) is measured using laser flash method in a Linseis XFA 600. Specific heat (C_p) is measured in a Linseis differential scanning calorimeter (DSC) using sapphire as the standard. Mass density (ρ) is calculated from the sample mass and dimensions. Hall coefficients (R_H) and resistivity (ρ) (Van der Pauw, 4-point probe) were measured simultaneously with a home-built instrument (Northwestern University) using a 2 T magnet with pressure-assisted Molybdenum contacts. The deviation of S is around 2%, electrical conductivity σ (5%) and thermal conductivity κ (5%). The combined uncertainty of zT $(S^2\sigma T/\kappa)$ is around 15%.

Structural Characterizations

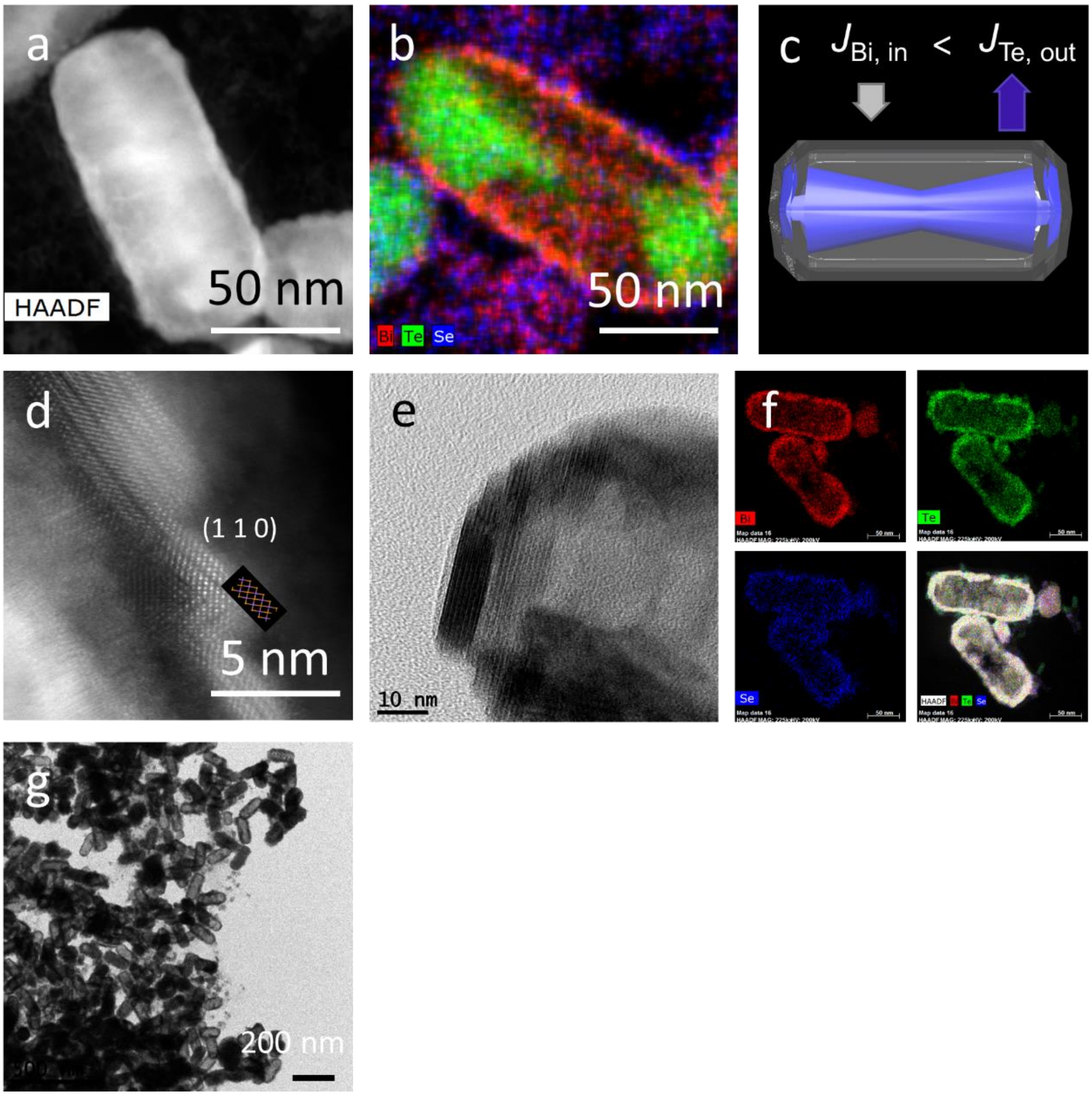

Figure S1. a) HAADF-STEM image of the Te@Bi-Se core-shell nanorod, b) EDS elemental mapping of a partially reacted Te@Bi-Se core-shell nanorod, c) schematic illustration of the Kirkendall effect, d) Cs-corrected HAADF-STEM image of a partially reacted Te@Bi-Se core-shell nanorod, the inset shows the atomic structure of (110) plane f Bi_2Te_3, e) HRTEM image and f) EDS elemental mapping of the hollow $Bi_2Te_{2.5}Se_{0.5}$ nanoshell. g) TEM image of the $Bi_2Te_{2.5}Se_{0.5}$ nanostructures after being incubated at 140ºC for 1h.

To further explain why the hollowing process initially takes place at the equatorial site of the nanorod, the nano-size effect should be taken into account. Considering the interface of Te/Bi_2Te_3/Bi, in which r_1 and r_2 are the radius of inner Te/Bi_2Te_3 and outer Bi_2Te_3/Bi interface, the growth rate of outer surface can be expressed as[1]

$$\frac{dr_2}{dt} \approx \frac{D_\beta}{kT}\left(-\frac{\Delta\mu_\beta}{\Delta r}\right)$$

Where $\Delta\mu_\beta = \Delta G_{Bi2Te3} + 2\Omega\left(\frac{\Upsilon_2}{r_2}+\frac{\Upsilon_1}{r_1}\right)$ and $\Delta r = r_2 - r_1$, γ_1 and γ_2 are the interfacial energies at the Te/Bi_2Te_3 and Bi_2Te_3/Bi interface, respectively, Ω is the atomic volume, ΔG_{Bi2Te3} is the formation energy of Bi_2Te_3 and it is negative here. When r_1 and r_2 are very small in the nanoscale, $\Delta\mu_\beta$ may approach zero or even become positive. Then the growth rate of outer surface (dr_2/dt) will become zero or even negative. Thus, this Gibbs-Thompson effect can inhibit the outer diffusion at the tip end where r_1 and r_2 are small. While at the equatorial site of the nanorod where r_1 and r_2 are larger, this effect is mitigated, allowing the outer diffusion process to happen.

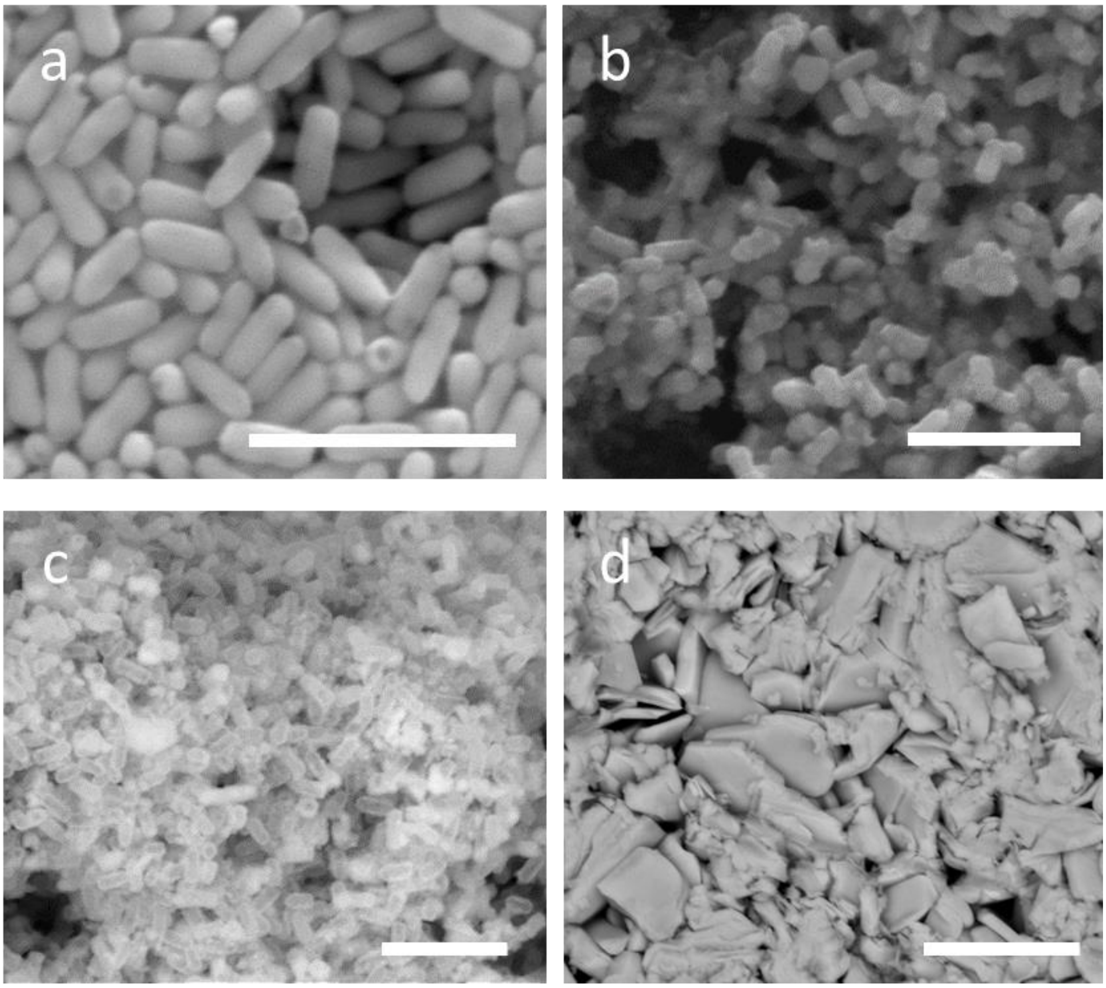

Figure S2. SEM images of a) Step 1, Te-Se nanorod, b) Step 2, Te@Bi-Se core-shell nanorod, c) Step 3, hollow $Bi_2Te_{2.5}Se_{0.5}$ nanoshell. The scale bars are 500 nm in a), b) and c). d) SEM image of the 400°C-sintered $Bi_2Te_{2.5}Se_{0.5}$ pellet, the scale bar is 2 µm.

Thermoelectric Property Data

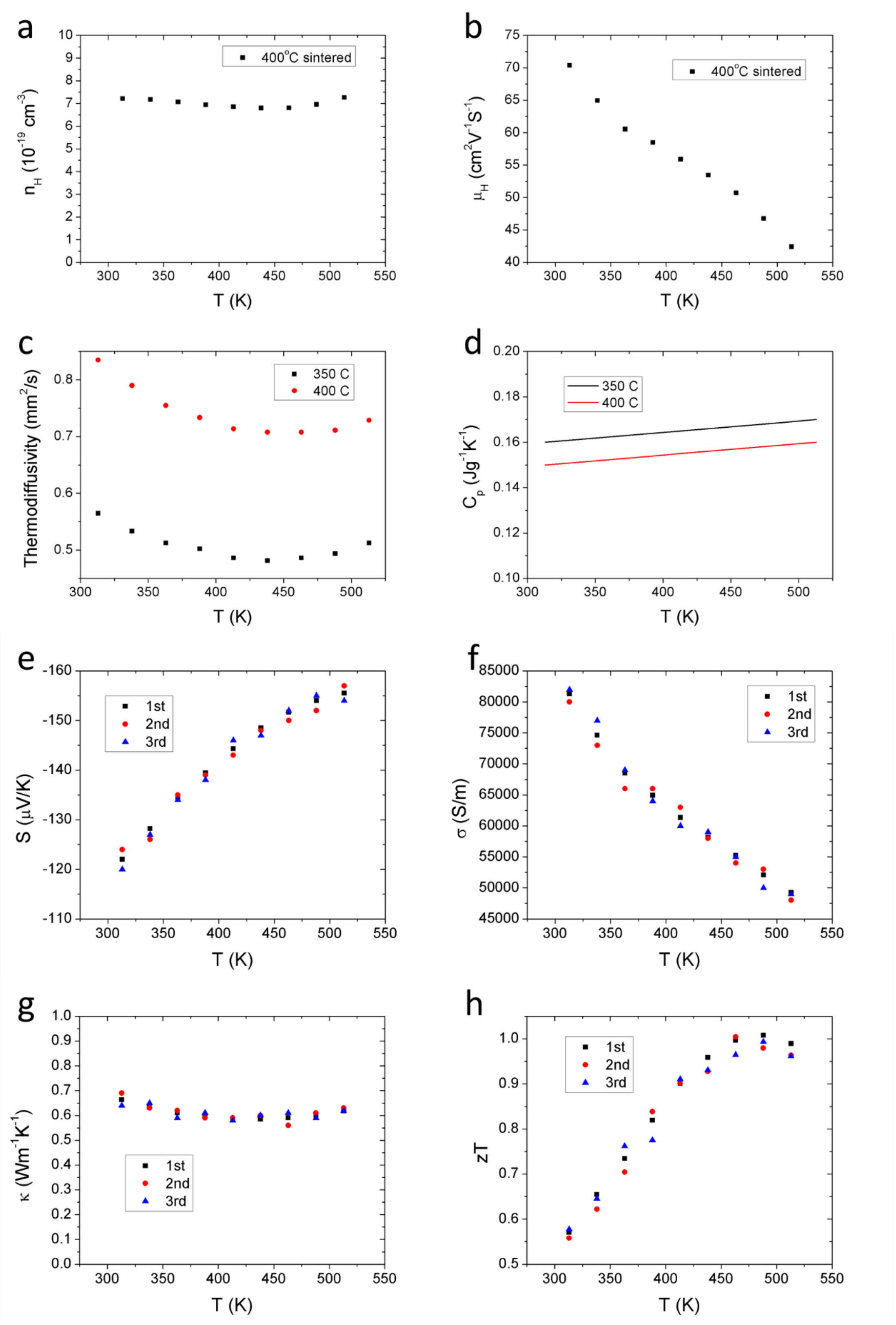

Figure S3. a) Hall electron concentration (n_H) and b) electron mobility (μ_H) of the 400^{o}C-sintered sample, c) thermal diffusivity and d) specific heat of the 350^{o}C- and 400^{o}C-sintered samples, e) Seebeck coefficient, f) electrical conductivity, g) thermal conductivity and h) zT of the 400^{o}C-sintered sample in repeated tests.

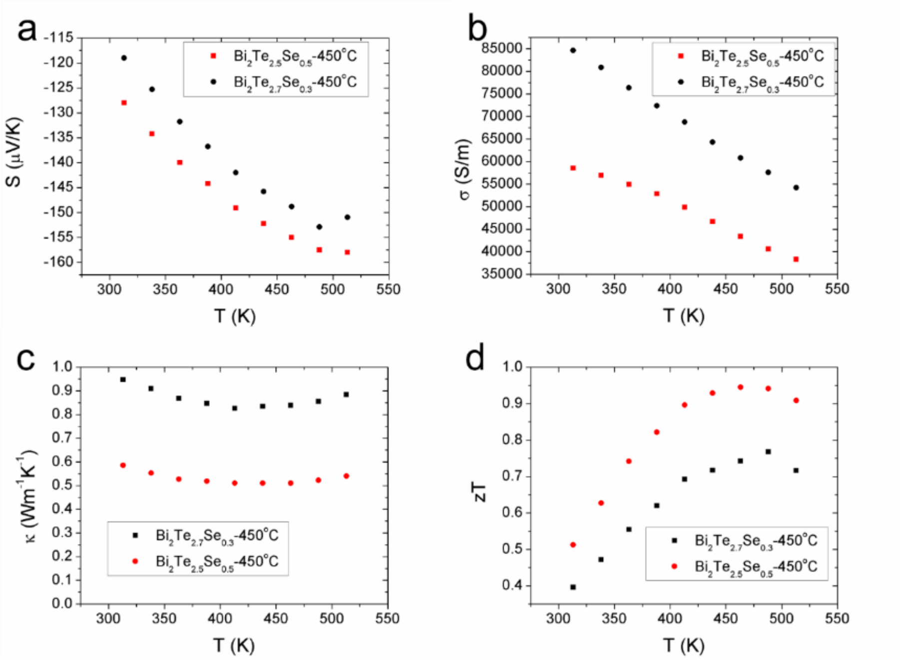

Figure S4. a) Seebeck coefficient, b) electrical conductivity, c) thermal conductivity and d) *zT* of 450^{o}C-sintered $Bi_2Te_{2.5}Se_{0.5}$ (red markers) and $Bi_2Te_{2.7}Se_{0.3}$ (black markers) samples.

Thermal Conductivity Modeling

The $\kappa_{l,f}$ is calculated according to:

$$\kappa_{l,f} = \frac{4\pi}{3}\frac{1}{(2\pi)^3}\sum_j\left[\frac{2}{3}\int_x + \frac{1}{3}\int_z\right]\frac{\hbar^2\omega^2(\mathbf{k},j)}{k_B T^2}\frac{e^{\frac{\hbar\omega(\mathbf{k},j)}{k_B T}}}{\left(e^{\frac{\hbar\omega(\mathbf{k},j)}{k_B T}}-1\right)^2}v^2(\mathbf{k},j)\tau_{ph}(\mathbf{k},j)k^2dk \tag{S1}$$

The integrals are done over k, the magnitude of wave-vector **k**. Since Bi_2Te_3 and Bi_2Se_3 are anisotropic, we choose the average of the 2 times of crystalline-in-plane (the integral with subscription *x*) and 1 time of crystalline-cross-plane thermal conductivities (the integral with subscription *z*). Note that the nano grain orientations in the nanocomposites are randomly distributed, and $\kappa_{l,f}$ is isotropic.

We notice that some literatures used the Debye-Callaway model to fit the thermal conductivity of Bi_2Te_3 nanostructures.[2] In their model, only the 3 acoustic phonon branches with linear dispersion relations have be considered, and thus it only works for the materials with zero or a few optical branches. The Bi_2Te_3 and Bi_2Se_3, however, have 3 dispersive acoustic branches and 12 optical branches, and it has been shown that the 4 low-energy optical phonon modes have a large contribution (50%) to the total lattice thermal conductivity. Thus, Debye-Callaway model is not suitable for Bi_2Te_3 and Bi_2Se_3 anymore. In our work, we include all the 3 acoustic branches and the 4 low-energy optical branches in our phonon BTE model.

In Eq.(S1), the phonon scattering rates induced by lattice anharmonicity (*anh*), Te-Se alloy mass disorder (*mass*), coupling between three-phonon and disorder scattering (*coupl*), dislocation core (*DC*), dislocation strain (*DS*), and grain boundaries (*b)* are expressed as:

$$\tau_{anh}^{-1}(\mathbf{k},j) = \frac{Ak_BT}{M_a v^2(\mathbf{k},j)}\frac{\gamma^2\omega^2(\mathbf{k},j)}{\omega_{\max}(j)}\exp\left(-\frac{\hbar\omega_{\max}(j)}{3k_BT}\right). \tag{S2}$$

$$\tau_{mass}^{-1}(\mathbf{k},j) = \frac{\pi}{2}g_{mass}\omega^2(\mathbf{k},j)DOS(\omega). \tag{S3}$$

$$\tau_{coupl}^{-1}(\mathbf{k},j) = \chi g_{mass}\tau_{anh}^{-1}. \tag{S4}$$

$$\tau_{DC}^{-1}(\mathbf{k},j) = N_D\frac{\bar{V}^{4/3}}{v^2(\mathbf{k},j)}\omega^3(\mathbf{k},j). \tag{S5}$$

$$\tau_{DS}^{-1}(\mathbf{k},j) = 0.6\xi N_D\omega(\mathbf{k},j). \tag{S6}$$

$$\tau_b^{-1}(\mathbf{k},j)=\begin{cases}\dfrac{v(\mathbf{k},j)}{D_{\parallel}}, & \textbf{in-plane mode}\\[2ex] \dfrac{v(\mathbf{k},j)}{D_{\perp}}, & \textbf{cross-plane mode}\end{cases} \quad . \qquad \text{(S7)}$$

For the anharmonic phonon scattering[3] in Eq. (S2), $\omega(\mathbf{k},j)$ and $v(\mathbf{k},v)$ and are the spectral phonon frequency and velocity, respectively. $\omega_{max}(v)$ is the maximum frequency of the phonon branch v. γ is the Grüneisen parameter with the values 1.5 and 1.4 for Bi_2Te_3 and Bi_2Se_3, respectively.[4] For our sample, $Bi_{2.02}Te_{2.56}Se_{0.44}$, γ is taken as the weighted average 1.48. M_a is the average atomic mass, given by

$$M_a=\frac{\alpha_{Bi}M_{Bi}+\alpha_{Te}M_{Te}+\alpha_{Se}M_{Se}}{\alpha_{Bi}+\alpha_{Te}+\alpha_{Se}}, \qquad \text{(S7)}$$

where α is the stoichiometric coefficient. The values of coefficient A , 1.21 and 1.7 for Bi_2Te_3 and Bi_2Se_3 respectively, are determined by the experimental room temperature lattice thermal conductivities values, 1.1 $Wm^{-1}K^{-1}$ and 1.2 $Wm^{-1}K^{-1}$ for pure Bi_2Te_3 and Bi_2Se_3, respectively[5].

For the mass disorder[6] in Eqn. (S3), $DOS(\omega)$ is the normalized phonon density of states. g_{mass} represents the alloying mass disorder induced by the mass difference between Te and Se atoms, given by

$$g_{mass}=\frac{\alpha_{Te}}{\alpha_{Te}+\alpha_{Se}}\left(1-\frac{M_{Te}}{\bar{M}_{TeSe}}\right)^2+\frac{\alpha_{Se}}{\alpha_{Te}+\alpha_{Se}}\left(1-\frac{M_{Se}}{\bar{M}_{TeSe}}\right)^2, \quad \bar{M}_{TeSe}=\frac{\alpha_{Te}M_{Te}+\alpha_{Se}M_{Se}}{\alpha_{Te}+\alpha_{Se}}. \qquad \text{(S8)}$$

Some literatures[2] used the Rayleigh model $\tau_{def}\sim\frac{g}{v^3}\omega^{-4}$ to evaluate the phonon-mass disorder scattering. It has been shown that, however, the Rayleigh model is a long-wavelength approximated model that only works for low-frequency phonons.[7] Equation (S2) has been shown to be more accurate in capturing the alloy and impurity scattering than the Rayleigh model due to the dispersive phonon branches.[7-8]

Since the mass-disorder, dislocation and boundary scattering have no temperature dependence, but the experimental k_{lat} shows a rapid decrease with increasing temperature, we attribute this to τ_{coupl}^{-1}, a temperature dependent scattering process. The coupling between the anharmonic phonon scattering and mass disorder scattering has also been observed in other alloy systems.[7, 9]

The dislocation scattering[2b, 10] is shown in Eqs. (S5-S6). N_D is the density of dislocations, $\bar{V}$ is the average atomic volume. ξ is calculated by

$$\xi=B_D^2(\gamma+\Delta\gamma)^2\left[\frac{1}{2}+\frac{1}{24}\left(\frac{1-2r}{1-r}\right)^2\left(1+\sqrt{2}\left(\frac{v_L}{v_T}\right)^2\right)^2\right], \qquad \text{(S9)}$$

in which B_D is the effective Burger's vector, r is the Poisson's ratio and $\Delta\gamma$ is the change in γ due to the dislocation strain, as given by

$$\Delta\gamma = \frac{V_{BT}K}{k_B T_a}\frac{\alpha_{Se}}{\alpha_{Te}+\alpha_{Se}}\left(\eta_V^2\gamma - \frac{1}{2}\eta_V\eta_M\right),\ \eta_V = \frac{V_{BS}-V_{BT}}{V_{BT}},\ \eta_M = \frac{M_{BT}-M_{BS}}{M_{BT}}. \qquad \text{(S10)}$$

Here K is the bulk modulus of Bi_2Te_3, T_a is the sample sintering temperature, V_{BS} and V_{BT} are the atomic volume of Bi_2Se_3 and Bi_2Te_3, and M_{BS} and M_{BT} are the atomic mass of Bi_2Se_3 and Bi_2Te_3.

The grain boundary scattering[6] in Eq. (S7) is determined by the grain diameter D.

Note that in our model, only χ is the fitting parameter (83 for 400°C -samples, 96 for 350°C -samples), and all the others are predetermined. The κ_{lat} is fitted according to the ($\kappa_{tot}-\kappa_e$) in the low temperatures (313 K-413 K) where bipolar effect does not appear (Figure S5). κ_e is estimated as $\kappa_e = L\sigma T$, where L is the Lorenz number, σ is the electrical conductivity. L is calculated through an empirical formula (L = 1.5 + exp(-|S|/116)) and was found to agree well with those calculated from single parabolic band model.[11]

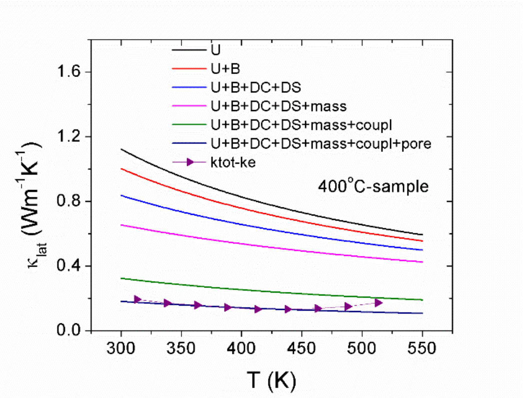

Figure S5. Calculated lattice thermal conductivity vs $\kappa_{tot} - \kappa_e$.

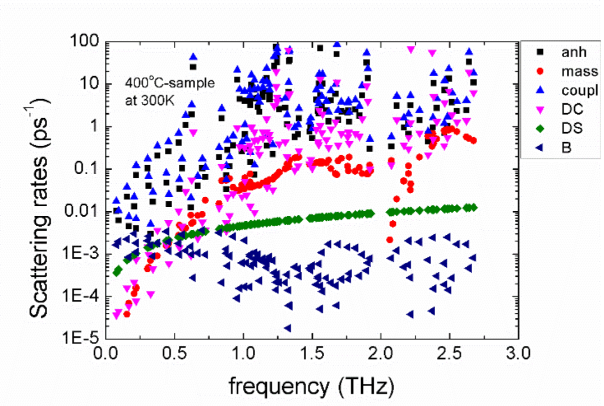

Figure S6. Scattering rates as a function of phonon frequency. The phonons suffer a broad-range phonon frequency scattering, e.g. the grain boundary scatter low-frequency phonons while the mass disorder (Te/Se), dislocation (DC and DS) and coupling between anharmonicity and mass disorder block the high frequency phonons more.

Table S1. The Pre-Determined Quantities and Parameters for κ_{lat} Calculation

	Quantities/parameters	**Values**	**Methods**
$\omega(\mathbf{k},j)$	Phonon frequency	Data set	First Principles (Ref. [12] &[13])
$v(\mathbf{k},j)$	Phonon group velocity	Data set	Calculated from $d\omega(\mathbf{k},j)/d\mathbf{k}$
$\omega_{max}(\mathbf{k},j)$	Max frequency	Data set	First Principles (Ref. [12] & [13])
$DOS(\omega)$	Phonon density of states	Data set	First Principles (Ref. [12] &[13])
$\alpha_{Bi}, \alpha_{Te}, \alpha_{Se}$	Atomic ratio	2.02:2.56:0.44	Experiment
A	Parameter	1.21 for Bi_2Te_3, 1.7 for Bi_2Se_3. ~1.28 used for our samples	Exp. κ_l of pure Bi_2Te_3 (Ref. [14])
ξ	Parameter	1.74×10^{-18} m^2 for 350 °C-samples 1.63×10^{-18} m^2 for 400 °C-samples	Calculated from Eq. (S9) based on Ref. [2b]
γ	Grüneisen parameter	1.5 for Bi_2Te_3, 1.4 for Bi_2Se_3. ~1.48 used for our samples	Ref. [4b] & [4a]
M_a	Average atomic mass	2.5918×10^{-25} kg	Calculated based on lattice structure
V_{BT}	atomic volume of Bi_2Te_3	33.77 Å^3	Calculated based on lattice structure
V_{BS}	atomic volume of Bi_2Se_3	28.4 Å^3	Calculated based on lattice structure
M_{BT}	atomic Mass of Bi_2Te_3	2.66×10^{-25} kg	Calculated based on lattice structure
M_{BS}	atomic Mass of Bi_2Se_3	2.18×10^{-25} kg	Calculated based on lattice structure
$\Delta\gamma$	Change of Grüneisen	1.0422	Eq. (S10)
B_D	effective Burger's vector	3.2 Å	Experiment
K	bulk modulus	37.4×10^9 Pa	Jenkins, J.; Ref. [15]
r	Poisson's ratio	0.4	Clin, T.; Ref. [16]
$\bar{V}$	Average atomic volume	33.77 Å^3 for Bi_2Te_3, 28.4 Å^3 for Bi_2Se_3, 32.98 Å^3 for our sample	Calculated based on lattice structure
g_{mass}	Mass disorder	0.0276	Eq. (S8)
N_D	Dislocation density	5.0×10^{11} cm^{-2} (350°C-sample), 7.6×10^{11} cm^{-2} (400°C-sample)	Experiment
$D_\perp, D_\parallel$	Grain diameter	350°C-sample: 1.2 μm (ab-plane), 250 nm (c-axis) 400°C-sample: 1.5 μm (ab-plane), 300 nm (c-axis)	Experiment

References in supporting information

[1] K. N. Tu, U. Gösele, *Appl. Phys. Lett.* **2005**, *86*, 093111.

[2] a) S. I. Kim, K. H. Lee, H. A. Mun, H. S. Kim, S. W. Hwang, J. W. Roh, D. J. Yang, W. H. Shin, X. S. Li, Y. H. Lee, G. J. Snyder, S. W. Kim, *Science* **2015**, *348*, 109-114; b) M. Hong, T. C. Chasapis, Z.-G. Chen, L. Yang, M. G. Kanatzidis, G. J. Snyder, J. Zou, *ACS Nano* **2016**, *10*, 4719-4727.

[3] G. A. Slack, S. Galginaitis, *Phys. Rev.* **1964**, *133*, A253-A268.

[4] a) X. Chen, H. D. Zhou, A. Kiswandhi, I. Miotkowski, Y. P. Chen, P. A. Sharma, A. L. Lima Sharma, M. A. Hekmaty, D. Smirnov, Z. Jiang, *Appl. Phys. Lett.* **2011**, *99*, 261912; b) D. Bessas, I. Sergueev, H. C. Wille, J. Perßon, D. Ebling, R. P. Hermann, *Phys. Rev. B* **2012**, *86*, 224301.

[5] W. Liu, K. C. Lukas, K. McEnaney, S. Lee, Q. Zhang, C. P. Opeil, G. Chen, Z. Ren, *Energy. Environ. Sci.* **2013**, *6*, 552-560.

[6] S.-i. Tamura, *Phys. Rev. B* **1983**, *27*, 858-866.

[7] T. Feng, B. Qiu, X. Ruan, *Phys. Rev. B* **2015**, *92*, 235206.

[8] J. Garg, N. Bonini, B. Kozinsky, N. Marzari, *Phys. Rev. Lett.* **2011**, *106*, 045901.

[9] P. Carruthers, *Phys. Rev.* **1962**, *126*, 1448-1452.

[10] P. G. Klemens, *Proc. Phys. Soc. Sec. A* **1955**, *68*, 1113.

[11] H.-S. Kim, Z. M. Gibbs, Y. Tang, H. Wang, G. J. Snyder, *APL Mater.* **2015**, *3*, 041506.

[12] V. Chis, I. Y. Sklyadneva, K. A. Kokh, V. A. Volodin, O. E. Tereshchenko, E. V. Chulkov, *Phys. Rev. B* **2012**, *86*, 174304.

[13] B.-T. Wang, P. Zhang, *Appl. Phys. Lett.* **2012**, *100*, 082109.

[14] D. P. Spitzer, *J. Phys. Chem. Solids* **1970**, *31*, 19-40.

[15] J. O. Jenkins, J. A. Rayne, R. W. Ure, *Phys. Rev. B* **1972**, *5*, 3171-3184.

[16] T. Clin, S. Turenne, D. Vasilevskiy, R. A. Masut, *J. Electron. Mater.* **2009**, *38*, 994-1001.